



Atomic Pd dispersion in triangular Cu nanosheets with dominant (111) plane as a tandem catalyst for highly efficient and selective electrodehalogenation

Huihuang Chen^a, Hongbo Li^a, Shaoqing Chen^{b,*}, Li Sheng^c, Zhirong Zhang^c, Wenlong Wu^c, Maohong Fan^d, Lianzhou Wang^{e,*}, Bo Yang^{a,*}

^a College of Chemistry and Environmental Engineering, Shenzhen University, Shenzhen 518060, PR China

^b Department of Materials Science and Engineering, Southern University of Science and Technology, Shenzhen 518055, PR China

^c Hefei National Laboratory for Physical Sciences at the Microscale, University of Science and Technology of China, Hefei 230026, PR China

^d Departments of Chemical and Petroleum Engineering, University of Wyoming, WY 82071, USA

^e School of Chemical Engineering, The University of Queensland, Brisbane, Qld 4072, Australia

ARTICLE INFO

Keywords:

Atomic Pd catalysis
Cu nanosheets
Hydrogen spillover
Electrochemical dehalogenation
Tribromophenol

ABSTRACT

Single-atom alloys (SAA) in which active metal atoms are atomically dispersed in an inert host possess unique geometric and electronic structures, and generally own higher catalytic performance than their monometallic counterparts. Whereas it is still challenging to facilitate synthesize well-defined single atoms embedded in single crystals dominated with a specific active plane. Herein, we synthesized Pd single atoms anchored in triangular Cu nanosheets (Pd₁Cu SAA) with dominant active (111) plane *via* wet chemical synthesis and galvanic replacement as a high-performance catalyst for the electrocatalytic hydrodehalogenation (ECHD) of the refractory tribromophenol. Based on intensive theoretical calculations and experimental work, a hydrogen spillover mechanism was firstly proposed and verified for the highly efficient and selective ECHD. Hydrogen spillover occurs from the hydrogen-rich Pd to the hydrogen-deficient Cu host with a marginal kinetic energy barrier due to the short reaction distance and the negligible interfacial resistance. Meanwhile, the strong metal-support interaction between Pd and peripheral Cu optimizes the adsorption of hydrogenated products to allow for the further catalytic reaction. Consequently, by decoupling the ECHD process into hydrogen adsorption, hydrogen spillover and hydrodebromination, Pd₁Cu SAA as a tandem catalyst completely reduced tribromophenol with high phenol selectivity. The intrinsic catalytic activity of Pd and Cu in Pd₁Cu SAA substantially outperforms their monometallic counterparts by 14.4 and 3.2 times, respectively. This work showcases that the atomic dispersion of noble metals in SAA offers a promising catalyst design strategy to attain unprecedented catalytic properties *via* isolating activation and desorption steps.

1. Introduction

Noble metals, particularly for Pd, have been widely utilized as heterogeneous catalysts in many important industrial processes such as organic synthesis and petroleum refining. The outstanding capability to generate and reserve highly reductive surface-adsorbed atomic hydrogen (*H) has rendered Pd “the Holy Grail” of hydrogenation catalysts, which have been employed in numerous reduction reaction hotspots in environment and renewable energy fields [1–4]. However, the over-strong affinity to adsorbed intermediates on Pd surface would disrupt the further catalytic reaction *via* poisoning or covering the active

sites [5]. Moreover, the high price, low abundance, and poor durability and selectivity of Pd restrict the large-scale application. In such context, many strategies have been implemented to further enhance its activity, selectivity, stability and atomic economy *via* altering electronic structure, tuning interfacial atomic arrangement, increasing dispersity or strengthening metal-support interaction by means of alloying [6–10], defect engineering [11], strain regulation [12], composition alternation [13,14], morphological control [15], or integration with supports (e.g., metal oxides/hydroxides/phosphides, graphene oxide, SiO₂, C₃N₄, SiC) [16–23].

Recently, single-atom alloys (SAA), in which Pd atoms are atomically

* Corresponding authors.

E-mail addresses: chensq3@sustech.edu.cn (S. Chen), l.wang@uq.edu.au (L. Wang), boyang@szu.edu.cn (B. Yang).

<https://doi.org/10.1016/j.apcatb.2023.122480>

Received 21 December 2022; Received in revised form 13 February 2023; Accepted 15 February 2023

Available online 16 February 2023

0926-3373/© 2023 Elsevier B.V. All rights reserved.

dispersed in a relatively inert host metal (Cu, Ag, Ni), have also been explored to further increase the atomic efficiency as well as tune their electronic and geometric structures [24]. Huge interest has been sparked continuously in discovering Pd-based SAA in the form of intermetallics [25], nanoparticles (NPs) [26–32], clusters [33] and nanowire [34] for diverse applications. Moreover, a few reports found that Pd could dissociate H_2 into *H which then spills over onto the Cu surface [35–37]. This phenomenon could allow Cu that cannot dissociate H_2 to harvest a large amount of highly active *H spilled from Pd atoms [38,39]. Especially, as Pd and Cu possess identical active (111) plane, it could diminish the diffusion length and interfacial resistance between the two metals, which might stimulate hydrogen spillover from Pd to Cu to enhance *H utilization, thereby boosting the intrinsic catalytic activity of each component [40–45]. Besides, the Cu host might weaken products adsorption relative to Pd NPs to promote the further catalytic process. However, it is still challenging nowadays to facilely synthesize well-defined Pd single atoms embedded in Cu single crystals particularly exposed with the highly active (111) plane.

On the other hand, the electrocatalytic hydrogenation can readily harness accessible, green and inexpensive protons from water and is one of the most fundamental reactions in energy and environmental scenarios, such as hydrodehalogenation [46,47], CO_2 reduction [48–51], nitrate reduction [34,52–54], O_2 reduction [55,56], N_2 reduction [57] and H_2O_2 production [55]. The electrocatalytic hydrodehalogenation (ECHD) can efficiently scissor the carbon-halogen bond of persistent halogenated organic compounds (e.g., organohalogen pesticides, flame retardants, transformer oil, et al.), which belong to one kind of the most toxic environmental pollutants. By doing so, the toxic halogen-containing functional groups can be destroyed to yield halogen-free products that can be more easily dealt with via subsequent cost-effective biodegradation. The ECHD process is an economical, environmentally friendly and low-carbon strategy to degrade many halogenated pollutants highly concerned in the field of environmental technology as it avoids high reagent costs and CO_2 greenhouse-gas emissions that are inevitable for commonly employed advanced oxidation processes. However, the key of the ECHD process lies in the elaborate and rational design of advanced electrocatalysts with specific structures to make it more economical, efficient and selective.

Herein, this work innovatively prepared a highly efficient and selective SAA electrocatalyst comprising Pd single atoms firmly anchored in Cu single crystals with the exceptional (111)-dominant plane (Pd_1Cu SAA) for the ECHD process. Tribromophenol (TBP) was selected as a model pollutant since it is the precursor of brominated flame retardants and also a typical disinfection by-product of drinking water. Moreover, its polyhalogenated structure and relatively large molecular size, compared to frequently employed probe molecules such as CO_2 , O_2 , N_2 , and NO_3^- , allow us to better elucidate the specific role of each reaction site on the surface of Pd_1Cu SAA during the multiple hydrodehalogenation process. Results show that the TBP removal rate was 100% with high phenol selectivity, dramatically outperforming the benchmark Pd NPs and the control Cu nanosheets (NSs). The intrinsic catalytic activity of Pd and Cu in Pd_1Cu SAA was significantly higher than their monometallic counterparts. Density functional theory (DFT) calculations and experimental data manifest that Pd_1Cu SAA not only optimized the hydrogen adsorption Gibbs free energy (ΔG_{H^+}) to induce hydrogen spillover, but also effectively tuned the affinity to hydrogenated products so as to facilitate the further hydrodehalogenation reaction.

2. Experimental section

2.1. Catalyst synthesis

2.1.1. Synthesis of Cu NSs

Cu NSs was synthesized via following a previously reported method [58]. Typically, deionized water (15 mL), copper nitrate trihydrate (Cu

$(NO_3)_2 \cdot 3H_2O$, 50 mg) and L-ascorbic acid (AA, 100 mg) were mixed in a vial (20 mL) under magnetic stirring to form a homogeneous solution at room temperature. AA not only served as the reductant but also protected Cu NSs from oxidation. Hexadecyltrimethylammonium bromide (CTAB) (100 mg) and hexamethylenetetramine (HMTA) (100 mg) were successively added in the obtained solution to form the complex compound of copper ions in a trigonal coordination geometry, followed by continuous stirring for 30 min. The vial was then capped and heated from room temperature to 80 °C with a ramp rate of 2 °C min^{-1} and kept for 3 h in an oil bath. Finally, the resultant Cu NSs was obtained by centrifugation and thoroughly washed with the ethanol/water mixture. Cu NSs was stored in ethanol to prevent oxidation except for other use.

2.1.2. Synthesis of Pd_1Cu SAA

Pd_1Cu SAA was obtained via a galvanic replacement method, driven by the relatively high standard reduction potential of Pd (Pd^{2+}/Cu , 0.83 V vs. SHE) relative to Cu (Cu^{2+}/Cu , 0.34 V vs. SHE). Cu NSs (10 mg) was uniformly dispersed in deionized water (20 mL) in a vial (20 mL) under sonication to yield a pink quicksand-like suspension. A desired amount (1.3/2.6/4.2 mL) of $Pd(NO_3)_2$ solution (1 g L^{-1}) was dropwise added in the above solution under the protection of nitrogen to obtain the corresponding sample $Pd_{0.03}Cu$ SAA, $Pd_{0.06}Cu$ SAA and $Pd_{0.1}Cu$ SAA. As $Pd_{0.06}Cu$ SAA (denoted as Pd_1Cu SAA thereafter) demonstrated the best catalytic performance (Fig. S1), the following work mainly focused on this sample. The solution turned into an opaque brown color once Pd(II) was added. After 30 min of stirring, the resulting Pd_1Cu SAA was centrifuged and washed with deionized water, and then dried in a vacuum oven at 60 °C for further use. The weight percent of Pd in Pd_1Cu SAA was 0.68 wt% determined by the inductively coupled plasma-mass spectrometry (ICP-MS).

2.2. Materials characterizations

The TEM image was taken with JEM-2100 & X-Max80 (JEOL) field-emission transmission electron microscope at an acceleration voltage of 200 kV. The AFM measurement was carried out using a Multimode 8 (Bruker) to obtain the thickness of Pd_1Cu SAA. XRD patterns were recorded on an Empyrean powder X-ray diffractometer (PANalytical). The aberration-corrected HAADF-STEM image was carried out on Talos F200X field-emission transmission electron microscope (Thermo Fisher Scientific) at the accelerating voltage of 200 kV. The corresponding EDS elemental mapping was performed on an ARM-200 F field-emission transmission electron microscope (JEOL) operated at an accelerating voltage of 200 kV. The weight percent of Pd in Pd_1Cu SAA was measured on a Trace Scan Advantage spectrometer (Atom scan Advantage, Thermo Jarrell Ash). A K-Alpha+ X-ray photoelectron spectroscopy (Thermo Fisher Scientific) was performed to analyze the composition and electronic state of the surface with monochromatic Al $K\alpha$ radiation. The CasaXPS software was used to interpret XPS data with the adventitious carbon peak calibrated to be 284.8 eV.

Hydrogen temperature-programed desorption (H_2 -TPD) was performed on Chembet Pulsar (Quantachrome Instrument, USA). For each test, 120 mg of the sample was prereduced at 200 °C using H_2 (50 sccm) for 120 min. Afterwards, the sample was cooled to 50 °C and cleaned with using argon gas to remove the weakly adsorbed H_2 . H_2 -TPD was conducted by heating the sample from 20 to 600 °C with a ramp rate of 2 °C min^{-1} under argon gas.

2.3. Electrochemical measurement

A CHI760E electrochemical station was used for the electrochemical hydrodebromination in a two-compartment H-type cell under ambient environment. The anode chamber and cathode chamber were separated by a proton-exchange membrane (Nafion 117) to avoid the oxidation of reduction products. The work electrode, counter electrode and reference electrode was catalyst-coated carbon paper, Pt mesh and Hg_2Cl_2/Hg ,

respectively. The work electrode was prepared by thoroughly mixing carbon black (2 mg), catalyst (2 mg), Nafion (40 μL), deionized water (0.5 mL) and ethanol (1.5 mL) under sonication for 1 h to gain a homogeneous catalyst ink, followed by loading onto one side of the carbon paper ($2\text{ cm} \times 2\text{ cm}$) to form a uniform film. For each test, 80 mL of 100 mM Na_2SO_4 solution with TBP (10 mg L^{-1}) was added in the cathode chamber and 80 mL of 200 mM H_2SO_4 + 100 mM Na_2SO_4 solution in the anode chamber. The temperature of catholyte and anolyte was constant (25 $^\circ\text{C}$) during the reaction. LSV curves were obtained in 100 mM Na_2SO_4 solution with TBP (10 mg L^{-1}) with a scanning rate of 5 mV s^{-1} . The recyclability of the catalyst was tested by replacing fresh catholyte after 4 h reaction using the same work electrode after rinsing.

2.4. Products analysis

Aliquots of 1 mL catholyte were taken by syringe at defined time points for HPLC analysis and filtered by 0.22 μm Milipore syringe filters. An Agilent high-performance liquid chromatography (HPLC) with a C18 column ($250 \times 4.6\text{ mm}^2$) and a UV detector at 295 nm was used to quantify TBP and hydrodebromination products with corresponding analytical standards at 25 $^\circ\text{C}$. A mixture of methanol and phosphoric acid (0.08%) (volume ratio:80/20) was employed as the mobile phase at a constant flow rate of 1.0 mL min^{-1} .

2.5. Theoretical calculations

The detailed information regarding density theory calculations has

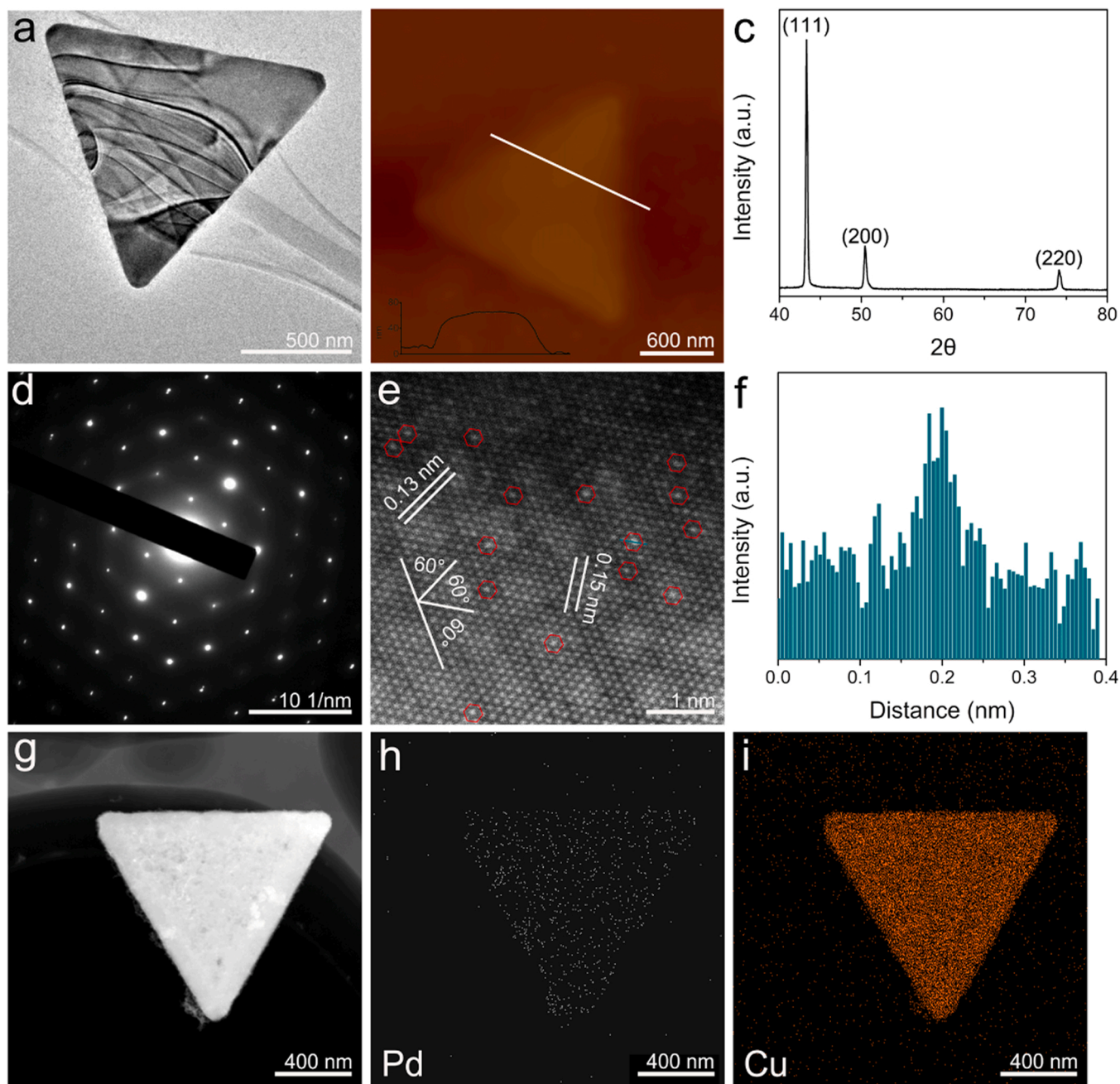


Fig. 1. (a) TEM image, (b) AFM image, (c) XRD pattern and (d) SAED pattern of triangular Cu NSs. (e) Aberration-corrected HAADF-STEM image of the basal plane of Cu NSs. Pd single atoms are marked by red hexagons. (f) The corresponding line intensity profile of Pd single atom taken along the cyan line in e. (g-i) HAADF-STEM image and the corresponding atomic-resolution EDS elemental mapping of Pd_1Cu SAA.

been provided in the [Supporting Information](#).

3. Results and discussion

3.1. Synthesis and material characterizations

Pd₁Cu SAA was synthesized *via* wet chemical reduction and subsequent galvanic replacement as illustrated in Schematic 1. The triangular Cu NSs was obtained through the chemical reduction of Cu(II) by AA in the presence of HMTA and CTAB [58]. The galvanic replacement reaction occurred after mixing Cu NSs and Pd(II) in aqueous solution to yield Pd₁Cu SAA. The detailed process can be referred in the Experimental section. Fig. 1a shows the typical transmission electron microscopy (TEM) image of the triangular Pd₁Cu SAA with an average edge length of $\sim 1.6 \pm 0.5 \mu\text{m}$. The line scan of the atomic force microscope (AFM) image (Fig. 1b) demonstrates that the thickness of Pd₁Cu SAA is ~ 50 nm. The dominant (111) peak of the X-ray diffraction (XRD) pattern (Fig. 1c) reveals the preferential growth of Cu atoms during the synthesis. The selective area electron diffraction (SAED) pattern further confirms the face-centred cubic (fcc) structure along the (111) direction (Fig. 1d). Scheme 1.

The lattice fringe spacing of 0.13 and 0.15 nm in the aberration-corrected high-angle annular dark field scanning transmission electron microscopy (HAADF-STEM) image (Fig. 1e) is attributed to the (200) and (220) plane of Pd₁Cu SAA, respectively. This suggests that the seen projection is indeed along the (111) direction. Pd single atoms, marked by red hexagons in Fig. 1e, can be easily discerned due to the heavier Z-contrast relative to Cu. Each Pd single atom lies in the centre of a hexagon consisted of six Cu atoms. The line intensity profile along the cyan line also demonstrates the atomically distributed Pd atoms in Cu NSs (Fig. 1f). The atomic-resolution elemental mapping *via* energy dispersive X-ray spectroscopy (EDS) further verifies the atomic and uniform dispersion of Pd atoms throughout the entire Cu NSs (Fig. 1g-i). With these observations, we conclude that Pd single atoms were successfully anchored in Cu NSs to obtain Pd₁Cu SAA, which was primarily enclosed by two (111) basal planes. This is extremely important for the efficient ECHD process for two reasons. Firstly, the (111) crystal plane of Pd catalysts is the catalytic active plane and Pd single atoms anchored in Cu (111) crystal plane might maintain its original properties and possess the highest catalytic activity[59]. Secondly, a single-crystal structure could minimize hydrogen diffusion length and interfacial resistance within the two components[40], which would enable facile $\ast\text{H}$ harvest for the ECHD process.

X-ray photoelectron spectroscopy (XPS) was employed to reveal the surface electronic states of Pd₁Cu SAA. The Cu 2p XPS spectrum of Pd₁Cu SAA shows two peaks located at 932.5 and 952.3 eV (Fig. 2a), which is assigned to Cu 2p_{3/2} and Cu 2p_{1/2}, respectively[60]. Notably, a negative shift was observed for the Cu 2p XPS spectrum of Pd₁Cu SAA compared to Cu NSs, indicating the electronic state of Cu altered after introducing Pd single atoms. Meanwhile, a positive shift was observed for the Pd 3d_{5/2} (336.67 eV) and Pd 3d_{3/2} (342.05 eV) XPS spectra of Pd₁Cu SAA with respect to Pd NPs (Fig. 2b). These results demonstrate that the combination of Pd single atoms and Cu NSs induced the strong metal-support interaction in Pd₁Cu SAA due to the inductive effect [61–63]. To visualize the interplay between Pd single atoms and Cu NSs,

we carried out DFT calculations. Based on the analysis of HAADF-STEM, SAED and XRD, the structural model of Pd₁Cu SAA was constructed and shown in Fig. 2c. The corresponding charge density difference plot was displayed in Fig. 2d. It can be vividly seen that a charge density rearrangement occurred at the (111) plane of Pd₁Cu SAA. The enriched electron cloud at the periphery of Pd single atoms visually depicts the electron transfer from Pd to the immediately adjacent Cu, thus leading to the increased valence state of Pd and the decreased valence state of Cu. The obviously observed charge density rearrangement coincides well with XPS results and jointly evidences the strong metal-support interaction in Pd₁Cu SAA, which would efficiently regulate the ECHD performance.

3.2. Electrocatalytic hydrodehalogenation performance

The ECHD performance of Pd₁Cu SAA was evaluated using TBP as a model pollutant in a typical H-type cell separated by a proton-exchange membrane at ambient conditions. At the potential of -0.5 V vs. SCE, only 63.7% TBP was reduced after 4 h (Fig. 3a). The removal rate of TBP was up to 100% when the potential increased to -0.6 V vs. SCE. Nevertheless, further increasing the potential to more negative values would not obviously boost the removal efficiency due to the intensified competing hydrogen evolution reaction. A lower pH value was beneficial for the ECHD possibly due to the facile formation of $\ast\text{H}$ (Fig. S2). The hydrodebrominated products were determined to be 2,6-dibromophenol (2,6-DBP), 2,4-dibromophenol (2,4-DBP), 2-bromophenol (2-BP), 4-bromophenol (4-BP) and phenol (Fig. 3b). The concentration of 2,6-DBP was the highest among the products except phenol throughout the reaction, which ascended at the initial stage and dropped to nearly zero after 4 h. Notably, phenol continued to accumulate and the TBP-to-phenol conversion ratio reached 92.6% after the reaction, implying the high selectivity of Pd₁Cu SAA for the deep hydrodebromination. Therefore, a stepwise mechanism (TBP \rightarrow 2,6-DBP \rightarrow 2-BP \rightarrow phenol) was deduced for the ECHD process of TBP (Fig. S3).

The ECHD performance of Pd₁Cu SAA was compared with the benchmark catalyst Pd NPs and the control sample Cu NSs (Fig. 3c). Surprisingly, the removal rate of TBP for Pd NPs and Cu NSs was merely 39% and 44%, respectively, at -0.6 V vs. SCE, which prominently underperforms that for Pd₁Cu SAA (100%). Kinetics analysis manifests that the degradation of TBP over Pd₁Cu SAA follows a pseudo-first-order reaction with a faster rate constant than Pd NPs and Cu NSs (Fig. 3d). The difference in the removal rate is even more remarkable when comparing the TOF values (Fig. 3e). The TOF value per Pd atom of Pd₁Cu SAA (Pd-Pd₁Cu) is 14.4 times that of Pd NPs. Likewise, the TOF value per Cu atom of Pd₁Cu SAA (Cu-Pd₁Cu) is 3.2-fold higher than that of Cu NSs. These results demonstrate that Pd₁Cu SAA could simultaneously enhance the intrinsic catalytic activity of Pd single atoms and the Cu host. It is worth noting that Pd₁Cu SAA is also applicable for high-concentrated TBP (Fig. S4). Pd₁Cu SAA maintained high catalytic activity (98.7%) and phenol selectivity (91%) after eight cycles (Fig. 3f), suggesting high durability for the efficient and selective ECHD of TBP. Pd₁Cu SAA remained intact after the reaction as evidenced by the HAADF-STEM image and the corresponding elemental mapping (Fig. S5).



Scheme 1. Schematic illustration of the synthesis of Pd₁Cu SAA *via* wet chemical reduction and subsequent galvanic replacement.

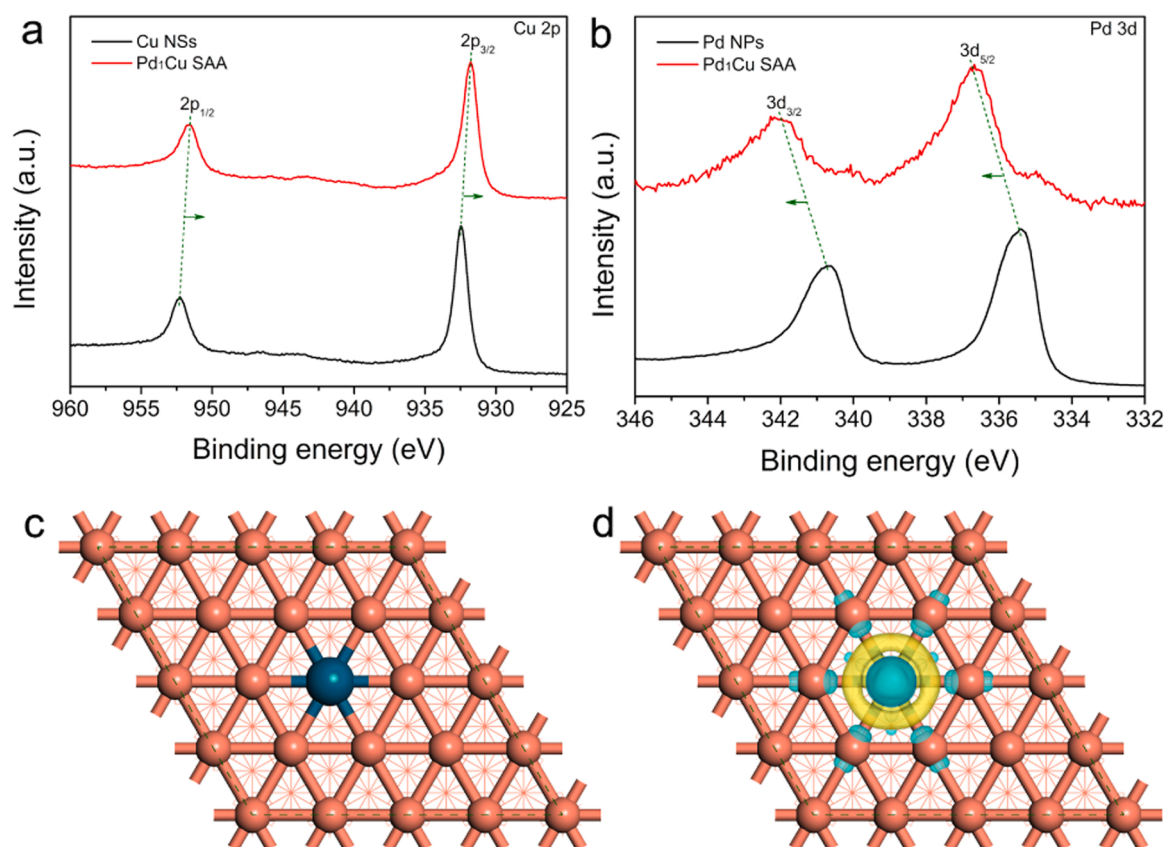


Fig. 2. (a) Cu 2p XPS spectra of Cu NSs and Pd₁Cu SAA. (b) Pd 3d XPS spectra of Pd NPs and Pd₁Cu SAA. (c) Structural model and (d) the corresponding charge density difference plot of Pd₁Cu SAA. The orange and dark cyan balls represent Cu and Pd atom, respectively. The yellow and blue regions present electron density accumulation and depletion, respectively.

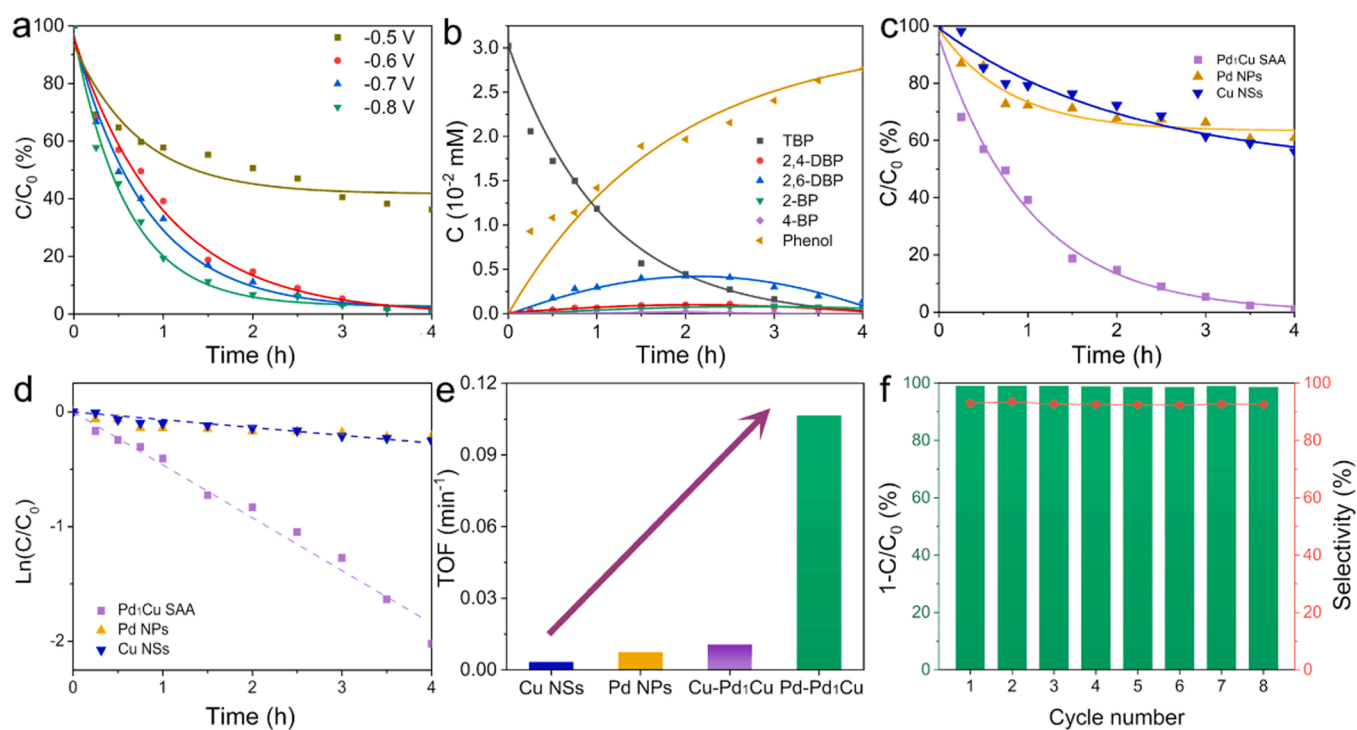


Fig. 3. (a) Degradation profiles of TBP with time under variant potentials vs. SCE. (b) Concentrations of TBP and the corresponding hydrodebrominated products. (c) Comparison of the catalytic activity of Pd₁Cu SAA, Pd NPs and Cu NSs for the electrocatalytic hydrodebromination of TBP. (d) TBP hydrodebromination kinetics over Pd₁Cu SAA, Pd NPs and Cu NSs. (e) TOF per metal atom for TBP hydrodebromination. (f) Conversion ratio and phenol selectivity of TBP using Pd₁Cu SAA over eight consecutive cycles.

3.3. Catalytic mechanism investigation

To unravel the origin of the outstanding intrinsic catalytic activity of Pd₁Cu SAA at the atomic scale, DFT calculations and linear sweep voltammetry (LSV) curves were further carried out. The pure Cu(111) and Pd(111) surface slab models were also constructed for the detailed mechanism investigation (Fig. S6). The (111) plane of Pd NPs was chosen because it is the catalytic active plane as well as the preferential plane based on the XRD result (Fig. S7). We conducted the density of states (DOS) calculations to elucidate the influence of Pd single atoms on the electronic structure of the Cu host (Fig. 4a). The DOS of Cu in Pd₁Cu SAA resembles that of Cu NSs with the same d-band centre of -2.3 eV due to the minor contribution of Pd single atoms compared to a multitude of Cu atoms, whereas it is worth noting that the DOS of Pd single atoms in Pd₁Cu SAA is significantly distinct from that of Pd NPs. Moreover, the d-band centre (-1.99 eV) of Pd single atoms is further away from the Fermi level compared to that (-1.81 eV) of Pd NPs, demonstrating that minimizing Pd NPs to the atomic level could dramatically weaken the adsorption capacity, which conforms with our initial hypothesis that the presence of the Cu host could weaken products adsorption relative to Pd NPs. We also calculated ΔG_{H^*} to assess the formation potential of H^* on Cu NSs, Pd₁Cu SAA and Pd NPs (Fig. 4b). It is found that Cu NSs own the weakest adsorption for H^* (0.036 eV), followed by Pd₁Cu SAA (0.022 eV) and Pd NPs (-0.44 eV). According to the Sabatier principle, the active site with a near-zero ΔG_{H^*} should facilitate the adsorption and desorption processes during the HER process. The ΔG_{H^*} of Pd₁Cu SAA is neither too strong to disrupt H^* desorption nor too weak to diminish H^* formation. Therefore, Pd₁Cu SAA was supposed to exhibit the highest catalytic activity for hydrogen evolution reaction, which is experimentally confirmed by the LSV curves (Fig. 4c). Specifically, Pd₁Cu SAA exhibited the highest current density over the potential range, implying the strongest electrocatalytic reductive capability. The onset potential (at the current density of -1 mA cm $^{-2}$) of Pd₁Cu SAA was substantially more positive than that of

Cu NSs and Pd NPs, indicating that H^* can be more readily formed via the Volmer step on Pd₁Cu SAA. The current density of Pd₁Cu SAA at the potential of -1.50 V is 2.2 times higher than that of Cu NSs. The considerably enhanced current density of Pd₁Cu SAA, compared to Cu NSs, could not be exclusively rationalized by the marginal difference in ΔG_{H^*} and nearly the same DOS. Hydrogen spillover might occur that accounted for the dramatic difference in the intrinsic catalytic activity and the LSV curves of Pd₁Cu SAA and Cu NSs. To corroborate the occurrence of hydrogen spillover, we conducted H₂-TPD and observed the color change in the mixture of Pd₁Cu SAA and WO₃ under constant potential electrolysis. Results show that a broad desorption response was observed in the H₂-TPD profile of Pd NPs (Fig. 4d). Notably, a sharp desorption peak at 331.7 °C appeared in the H₂-TPD profile of Pd₁Cu SAA, which indicates the occurrence of hydrogen spillover [37]. Additionally, the mixture of Pd₁Cu SAA and WO₃ changed color from yellow to dark blue due to the formation of H₂WO₃ via the rapid reaction between spilled-over hydrogen and WO₃ under potentiostatic conditions (Fig. S8) [40]. Combining the above analysis, it can be concluded that hydrogen spillover did take place on Pd₁Cu SAA.

To further approve the occurrence of hydrogen spillover, we employed DFT calculations to investigate the kinetic energy barrier during the process over Pd₁Cu SAA (Fig. 4e; Table S1). Hydrogen generally spills from the hydrogen-rich component with a negative ΔG_{H^*} to the hydrogen-poor component with a positive ΔG_{H^*} . For the DFT calculations, H^* was initially set to be linearly and vertically adsorbed atop Pd single atoms at position S1 (Fig. S9) owing to the strong hydrogen adsorption capability. During the structure optimization, H^* spontaneously migrated from position S1 to position S2 (Fig. S10) with a Gibbs free-energy change of -0.36 eV in the threefold fcc hollow site with one Pd atom and two neighboring Cu atoms (Supplementary Video S1), in agreement with previous studies [64,65]. These results indicate that the migration of H^* from position S1 to position S2 is a kinetically favorable process. We subsequently calculated the kinetic energy barrier of hydrogen spillover from S2 to S3 (Fig. S11) in which H^* was located in

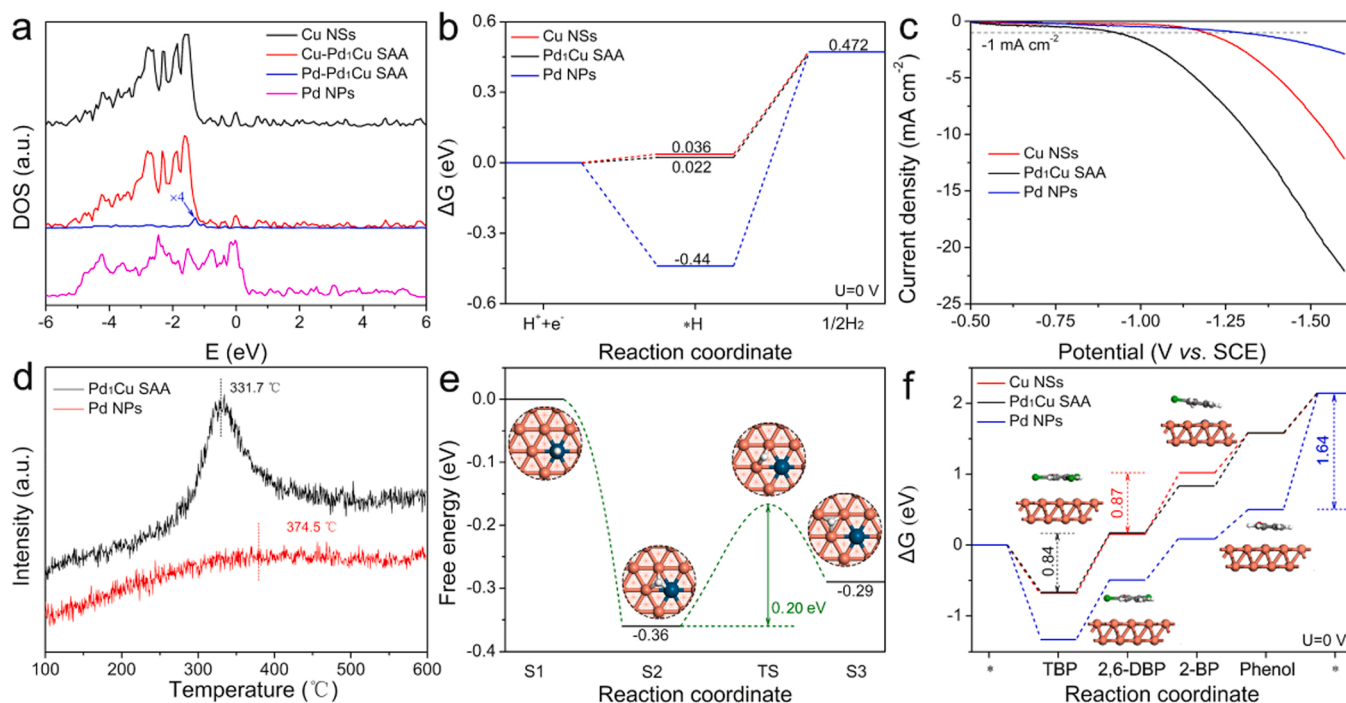


Fig. 4. (a) DOS of Cu NSs, Pd₁Cu SAA and Pd NPs. (b) Gibbs free-energy diagram for hydrogen adsorption on Cu NSs, Pd₁Cu SAA and Pd NPs. (c) LSV curves of Cu NSs, Pd₁Cu SAA and Pd NPs in a N₂-saturated 0.1 M Na₂SO₄ solution with a scan rate of 5 mV s $^{-1}$. (d) H₂-TPD profiles of Pd₁Cu SAA and Pd NPs. (e) The kinetic energy barrier of hydrogen spillover/migration process over Pd₁Cu SAA (S1: H^* linearly and vertically located on a single Pd atom; S2: H^* located on the threefold fcc hollow site of one Pd atom and two adjacent Cu atoms; TS: the transition state; S3: H^* located on the threefold fcc hollow site of three Cu atoms close to S2). (f) Gibbs free-energy diagram for the TBP hydrodebromination to phenol at pH = 4 on Cu NSs, Pd₁Cu SAA and Pd NPs.

the threefold fcc hollow site of three most closely adjacent Cu atoms (Supplementary Video S2). Although a slight positive kinetic energy barrier of 0.20 eV is required to overcome the transient state (TS), the hydrogen spillover from S1 to S3 was a free-energy downhill process as a whole. Moreover, the kinetic energy barrier (0.20 eV) of hydrogen spillover from S1 to S3 is obviously lower than the theoretical overpotential (0.91 eV) for hydrogen evolution reaction on Pd NPs (Fig. 4b). The above-mentioned DFT calculations and experimental results systematically verified the occurrence of hydrogen spillover over Pd₁Cu SAA via the synergy of dual-function active sites.

Supplementary material related to this article can be found online at [doi:10.1016/j.apcatb.2023.122480](https://doi.org/10.1016/j.apcatb.2023.122480).

Supplementary material related to this article can be found online at [doi:10.1016/j.apcatb.2023.122480](https://doi.org/10.1016/j.apcatb.2023.122480).

The ECHD process of TBP on Cu NSs, Pd₁Cu SAA and Pd NPs was also investigated using DFT calculations based on the proposed stepwise degradation pathway (Table S2). The Gibbs free-energy diagram was displayed in Fig. 4f. The rate-determining step (RDS) over Pd₁Cu SAA was the formation of 2,6-DBP, which is in line with experimental data (Fig. 3b). The energy barrier of the RDS for Pd₁Cu SAA was 0.84 eV, smaller than that for Cu NSs (0.87 eV) and Pd NPs (1.64 eV), further demonstrating the higher intrinsic catalytic activity. The RDS for Cu NSs and Pd NPs was the transformation of 2,6-DBP to 2-BP and the desorption of phenol, respectively. Notably, the combination of Pd single atoms and Cu NSs significantly weakened the adsorption of phenol compared to Pd NPs, which is vital to refresh the catalytic surface for the further reaction. That explains well why TBP degradation over Pd NPs reached a plateau after 2 h (Fig. 3c). The stronger adsorption of phenol over Pd NPs, compared to Pd₁Cu SAA and Cu NSs, can be also rationalized by the optimized adsorption configurations of hydrogenated products (Fig. S12–S14). Therefore, hydrogen spillover and adsorption optimization concurrently boosted the ECHD process of TBP over Pd₁Cu SAA.

The electrocatalytic debromination process of TBP over Pd₁Cu SAA was schematically illustrated in Fig. 5. Hydrogen spillover occurs at the interface between Pd single atoms and the Cu host. Pd single atoms initiate facile proton enrichment due to the strong proton adsorption, followed by hydrogen spillover from Pd to peripheral Cu due to the strong metal-support interaction, and further to the fcc hollow site of three most closely adjacent Cu atoms thanks to the marginal kinetic energy barrier that stems from the short reaction distance and the interface-free feature on Pd₁Cu SAA. Besides, the atomic dispersion of Pd in Cu NSs facilitates the desorption of phenol that is beneficial for the sustained domino ECHD process. In such context, the ECHD process was decoupled into hydrogen adsorption, hydrogen spillover, and hydrodehalogenation that contribute to the observed higher intrinsic catalytic performance.

4. Conclusions

To summarize, we have successfully synthesized a SAA catalyst Pd₁Cu SAA dominated with the highly active (111) plane via wet chemical synthesis and subsequent galvanic replacement. The strong metal-support interaction in Pd₁Cu SAA induces the charge transfer from Pd single atoms to circumjacent Cu atoms, and weakens the over-strong affinity to hydrogenated products, which facilitates the further catalytic reaction. DFT calculations and experimental results demonstrate that hydrogen spillover occurs from the hydrogen-enriched Pd to the hydrogen-poor Cu. By decoupling the ECHD process into hydrogen adsorption, hydrogen spillover and hydrodehalogenation, Pd₁Cu SAA as a tandem catalyst displays an exceptional catalytic performance for the electrocatalytic hydrodebromination of TBP with nearly 100% removal rate and phenol selectivity. The intrinsic catalytic activity of Pd and Cu in Pd₁Cu SAA is greatly enhanced with a reduced energy barrier in comparison to their monometallic counterparts. This proof-of-concept work not only provides the atomic-scale understanding of hydrogen spillover over Pd₁Cu SAA for the ECHD process, but also presents

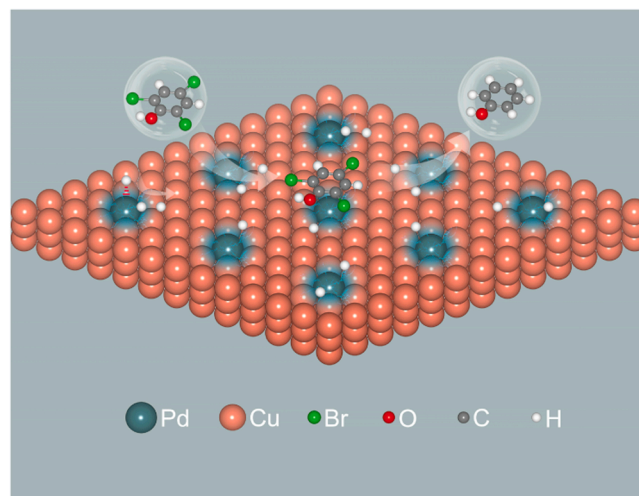


Fig. 5. Schematic illustration of the electrocatalytic hydrodebromination process of TBP over Pd₁Cu SAA via hydrogen spillover.

opportunities to design advanced electrocatalysts via integrating multiple functional sites for other various catalytic applications.

Supporting information

DFT calculations, and corresponding additional data including XRD, DFT models, adsorption configurations, and supplementary videos.

CRediT authorship contribution statement

Huihuang Chen: Project administration, Conceptualization, Data curation, Formal analysis, Funding acquisition, Methodology, Writing - original draft. **Hongbo Li:** Validation, Methodology, Formal analysis. **Shaoqing Chen:** Formal analysis, Supervision, Funding acquisition. **Li Sheng:** Software. **Zhirong Zhang:** Formal analysis. **Wenlong Wu:** Formal analysis. **Maohong Fan:** Formal analysis. **Lianzhou Wang:** Formal analysis, Writing - review & editing, Project administration. **Bo Yang:** Formal analysis, Methodology, Supervision, Funding acquisition, Writing - review & editing, Project administration.

Declaration of Competing Interest

The authors declare that they have no known competing financial interests or personal relationships that could have appeared to influence the work reported in this paper.

Data Availability

Data will be made available on request.

Acknowledgment

This work was financially supported by the National Natural Science Foundation of China (22005288 and 22176131) and the Key Project of Basic Research of Shenzhen (JCYJ20220818095601002).

Notes

The authors declare no competing interests.

Author contributions

All authors discussed the results and contributed to the manuscript.

Appendix A. Supporting information

Supplementary data associated with this article can be found in the online version at [doi:10.1016/j.apcatb.2023.122480](https://doi.org/10.1016/j.apcatb.2023.122480).

References

- [1] B. Yang, G. Yu, J. Huang, *Environ. Sci. Technol.* 41 (2007) 7503–7508.
- [2] B.P. Chaplin, M. Reinhard, W.F. Schneider, C. Schüth, J.R. Shapley, T. J. Strathmann, C.J. Werth, *Environ. Sci. Technol.* 46 (2012) 3655–3670.
- [3] Y. Zhou, G. Zhang, Q. Ji, W. Zhang, J. Zhang, H. Liu, J. Qu, *Environ. Sci. Technol.* 53 (2019) 11383–11390.
- [4] R. Liu, H. Zhao, X. Zhao, Z. He, Y. Lai, W. Shan, D. Bekana, G. Li, J. Liu, *Environ. Sci. Technol.* 52 (2018) 9992–10002.
- [5] Y. Peng, M. Cui, Z. Zhang, S. Shu, X. Shi, J.T. Brosnahan, C. Liu, Y. Zhang, P. Godbold, X. Zhang, F. Dong, G. Jiang, S. Zhang, *ACS Catal.* 9 (2019) 10803–10811.
- [6] Y. Zhou, G. Zhang, Q. Ji, W. Zhang, J. Zhang, H. Liu, J. Qu, *Environ. Sci. Technol.* 53 (2019) 11383–11390.
- [7] M. Luo, Z. Zhao, Y. Zhang, Y. Sun, Y. Xing, F. Lv, Y. Yang, X. Zhang, S. Hwang, Y. Qin, J.-Y. Ma, F. Lin, D. Su, G. Lu, S. Guo, *Nature* 574 (2019) 81–85.
- [8] X. Fu, J. Liu, S. Kanchanakungwankul, X. Hu, Q. Yue, D.G. Truhlar, J.T. Hupp, *Y. Kang, Nano Lett.* 21 (2021) 5620–5626.
- [9] X. Zhou, K. Li, Y. Lin, L. Song, J. Liu, Y. Liu, L. Zhang, Z. Wu, S. Song, J. Li, H. Zhang, *Angew. Chem. Int. Ed.* 59 (2020) 13568–13574.
- [10] H. Wang, Q. Luo, W. Liu, Y. Lin, Q. Guan, X. Zheng, H. Pan, J. Zhu, Z. Sun, S. Wei, J. Yang, J. Lu, *Nat. Commun.* 10 (2019) 4998.
- [11] R. Liu, H. Zhao, X. Zhao, Z. He, Y. Lai, W. Shan, D. Bekana, G. Li, J. Liu, *Environ. Sci. Technol.* 52 (2018) 9992–10002.
- [12] H. Huang, H. Jia, Z. Liu, P. Gao, J. Zhao, Z. Luo, J. Yang, J. Zeng, *Angew. Chem. Int. Ed.* 56 (2017) 3594–3598.
- [13] Y. Jia, T.-H. Huang, S. Lin, L. Guo, Y.-M. Yu, J.-H. Wang, K.-W. Wang, S. Dai, *Nano Lett.* 22 (2022) 1391–1397.
- [14] J. Xu, D. Gao, H. Yu, P. Wang, B. Zhu, L. Wang, J. Fan, *Chin. J. Catal.* 43 (2022) 215–225.
- [15] H. Jung, M.E. King, M.L. Personick, *Curr. Opin. Colloid* 40 (2019) 104–117.
- [16] J. Li, M. Li, J. Li, S. Wang, G. Li, X. Liu, *Appl. Catal. B* 282 (2021) 119518.
- [17] T. Richards, J.H. Harthy, R.J. Lewis, A.G.R. Howe, G.M. Suldecki, A. Folli, D. J. Morgan, T.E. Davies, E.J. Loveridge, D.A. Crole, J.K. Edwards, P. Gaskin, C. J. Kiely, Q. He, D.M. Murphy, J.-Y. Maillard, S.J. Freakley, G.J. Hutchings, *Nat. Catal.* 4 (2021) 575–585.
- [18] A. Pei, G. Li, L. Zhu, Z. Huang, J. Ye, Y.-C. Chang, S.M. Osman, C.-W. Pao, Q. Gao, B.H. Chen, R. Luque, *Adv. Funct. Mater.* (2022), 2208587.
- [19] L. Feng, J. Chang, K. Jiang, H. Xue, C. Liu, W.-B. Cai, W. Xing, J. Zhang, *Nano Energy* 30 (2016) 355–361.
- [20] J. Wang, S.A. Kondrat, Y. Wang, G.L. Brett, C. Giles, J.K. Bartley, L. Lu, Q. Liu, C. J. Kiely, G.J. Hutchings, *ACS Catal.* 5 (2015) 3575–3587.
- [21] H. Wang, Q. Luo, W. Liu, Y. Lin, Q. Guan, X. Zheng, H. Pan, J. Zhu, Z. Sun, S. Wei, J. Yang, J. Lu, *Nat. Commun.* 10 (2019) 4998.
- [22] S. Cao, Y. Chen, H. Wang, J. Chen, X. Shi, H. Li, P. Cheng, X. Liu, M. Liu, L. Piao, *Joule* 2 (2018) 549–557.
- [23] C. Chu, D. Huang, S. Gupta, S. Weon, J. Niu, E. Stavitski, C. Muhich, J.-H. Kim, *Nat. Commun.* 12 (2021) 5179.
- [24] R.T. Hannagan, G. Giannakakis, M. Flytzani-Stephanopoulos, E.C.H. Sykes, *Chem. Rev.* 120 (2020) 12044–12088.
- [25] Y. Ji, Z. Chen, R. Wei, C. Yang, Y. Wang, J. Xu, H. Zhang, A. Guan, J. Chen, T.-K. Sham, J. Luo, Y. Yang, X. Xu, G. Zheng, *Nat. Catal.* 5 (2022) 251–258.
- [26] F. Xing, J. Jeon, T. Toyao, K.-I. Shimizu, S. Furukawa, *Chem. Sci.* 10 (2019) 8292–8298.
- [27] L. Zhang, H. Liu, S. Liu, M.N. Banis, Z. Song, J. Li, L. Yang, M. Markiewicz, Y. Zhao, R. Li, M. Zheng, S. Ye, Z.-J. Zhao, G.A. Botton, X. Sun, *ACS Catal.* 9 (2019) 9350–9358.
- [28] C.-H. Chen, D. Wu, Z. Li, R. Zhang, C.-G. Kuai, X.-R. Zhao, C.-K. Dong, S.-Z. Qiao, H. Liu, X.-W. Du, *Adv. Energy Mater.* 9 (2019), 1803913.
- [29] C.J. Wrasman, A. Boubnov, A.R. Riscoe, A.S. Hoffman, S.R. Bare, M. Cargnello, *J. Am. Chem. Soc.* 140 (40) (2018) 12930–12939.
- [30] X. Zhang, G. Cui, H. Feng, L. Chen, H. Wang, B. Wang, X. Zhang, L. Zheng, S. Hong, M. Wei, *Nat. Commun.* 10 (2019) 5812.
- [31] H. Wang, Q. Luo, W. Liu, Y. Lin, Q. Guan, X. Zheng, H. Pan, J. Zhu, Z. Sun, S. Wei, J. Yang, J. Lu, *Nat. Commun.* 10 (2019) 4998.
- [32] P. Aich, H. Wei, B. Basan, A.J. Kropf, N.M. Schweitzer, C.L. Marshall, J.T. Miller, R. Meyer, *J. Phys. Chem. C* 119 (2015) 18140–18148.
- [33] X.L. Du, X.L. Wang, Y.H. Li, Y.L. Wang, J.J. Zhao, L.J. Fang, L.R. Zheng, H. Tong, H. G. Yang, *Chem. Commun.* 53 (2017) 9402–9405.
- [34] F.-Y. Chen, Z.-Y. Wu, S. Gupta, D.J. Rivera, S.V. Lambeets, S. Pecaut, J.Y.T. Kim, P. Zhu, Y.Z. Finrock, D.M. Meira, G. King, G. Gao, W. Xu, D.A. Cullen, H. Zhou, Y. Han, D.E. Perea, C.L. Muhich, H. Wang, *Nat. Nanotechnol.* 17 (2022) 759–767.
- [35] H.L. Tierney, A.E. Baber, J.R. Kitchin, E.C.H. Sykes, *Phys. Rev. Lett.* 103 (2009), 246102.
- [36] M.T. Darby, R. Réocreux, E.C.H. Sykes, A. Michaelides, M. Stamatakis, *ACS Catal.* 8 (2018) 5038–5050.
- [37] G. Kyriakou, M.B. Boucher, A.D. Jewell, E.A. Lewis, T.J. Lawton, A.E. Baber, H. L. Tierney, M. Flytzani-Stephanopoulos, E.C.H. Sykes, *Science* 335 (2012) 1209–1212.
- [38] Y. Zhang, X. Chen, W. Wang, L. Yin, J.C. Crittenden, *Appl. Catal. B* 310 (2022), 121346.
- [39] M.T. Greiner, T.E. Jones, S. Beeg, L. Zwiener, M. Scherzer, F. Girgsdies, S. Piccinin, M. Armbrüster, A. Knop-Gericke, R. Schlögl, *Nat. Chem.* 10 (2018) 1008–1015.
- [40] J. Dai, Y. Zhu, Y. Chen, X. Wen, M. Long, X. Wu, Z. Hu, D. Guan, X. Wang, C. Zhou, Q. Lin, Y. Sun, S.-C. Weng, H. Wang, W. Zhou, Z. Zhao, *Nat. Commun.* 13 (2022) 1189.
- [41] F.R. Lucci, M.T. Darby, M.F.G. Matterna, C.J. Ivimey, A.J. Therrien, A. Michaelides, M. Stamatakis, E.C.H. Sykes, *J. Phys. Chem. Lett.* 7 (2016) 480–485.
- [42] D.V. Esposito, I. Levin, T.P. Moffat, A.A. Talin, *Nat. Mater.* 12 (2013) 562–568.
- [43] J. Li, H.-X. Liu, W. Gou, M. Zhang, Z. Xia, S. Zhang, C.-R. Chang, Y. Ma, Y. Qu, *Environ. Sci. Technol.* 12 (2019) 2298–2304.
- [44] M. Xiong, Z. Gao, Y. Qin, *ACS Catal.* 11 (2021) 3159–3172.
- [45] W.C. Conner Jr, J.L. Falconer, *Chem. Rev.* 95 (1995) 759–788.
- [46] B. Yang, H. Li, Z. Zhang, K. Xiao, M. Yang, F. Zhang, M. Wang, X. Guo, Q. Li, W. Fu, R. Si, L. Wang, H. Chen, *Chem. Eng. J.* 427 (2022), 131719.
- [47] Y. Xu, Z. Yao, Z. Mao, M. Shi, X. Zhang, F. Cheng, H.B. Yang, H.B. Tao, B. Liu, *Appl. Catal. B* 277 (2020), 119057.
- [48] H. Chen, X. Guo, X. Kong, Y. Xing, Y. Liu, B. Yu, Q.-X. Li, Z. Geng, R. Si, J. Zeng, *Green. Chem.* 22 (2020) 7529–7536.
- [49] F.P. García de Arquer, C.-T. Dinh, A. Ozden, J. Wicks, C. McCallum, A.R. Kirmani, D.-H. Nam, C. Gabardo, A. Seifitokaldani, X. Wang, Y.C. Li, F. Li, J. Edwards, L. J. Richter, S.J. Thorpe, D. Sinton, E.H. Sargent, *Science* 367 (2020) 661–666.
- [50] K. Jiang, R.B. Sandberg, A.J. Akey, X. Liu, D.C. Bell, J.K. Nørskov, K. Chan, H. Wang, *Nat. Catal.* 1 (2018) 111–119.
- [51] C.-T. Dinh, T. Burdyny, M.G. Kibria, A. Seifitokaldani, C.M. Gabardo, F.P. García de Arquer, A. Kiani, J.P. Edwards, P. De Luna, O.S. Bushuyev, C. Zou, R. Quintero-Bermudez, Y. Pang, D. Sinton, E.H. Sargent, *Science* 360 (2018) 783–787.
- [52] H. Chen, C. Zhang, L. Sheng, M. Wang, W. Fu, S. Gao, Z. Zhang, S. Chen, R. Si, L. Wang, B. Yang, *J. Hazard. Mater.* 434 (2022), 128892.
- [53] Y. Yao, L. Zhao, J. Dai, J. Wang, C. Fang, G. Zhan, Q. Zheng, W. Hou, L. Zhang, *Angew. Chem. Int. Ed.* 61 (2022), e202208215.
- [54] J. Li, G. Zhan, J. Yang, F. Quan, C. Mao, Y. Liu, B. Wang, F. Lei, L. Li, A.W.M. Chan, L. Xu, Y. Shi, Y. Du, W. Hao, P.K. Wong, J. Wang, S.-X. Dou, L. Zhang, J.C. Yu, *J. Am. Chem. Soc.* 142 (2020) 7036–7046.
- [55] C. Xia, Y. Xia, P. Zhu, L. Fan, H. Wang, *Science* 366 (2019) 226–231.
- [56] X. Huang, Z. Zhao, L. Cao, Y. Chen, E. Zhu, Z. Lin, M. Li, A. Yan, A. Zettl, Y. M. Wang, X. Duan, T. Mueller, Y. Huang, *Science* 348 (2015) 1230–1234.
- [57] Y. Liu, Q. Li, X. Guo, X. Kong, J. Ke, M. Chi, Q. Li, Z. Geng, J. Zeng, *Adv. Mater.* 32 (2020), 1907690.
- [58] W. Luc, X. Fu, J. Shi, J.-J. Lv, M. Jouny, B.H. Ko, Y. Xu, Q. Tu, X. Hu, J. Wu, Q. Yue, Y. Liu, F. Jiao, Y. Kang, *Nat. Catal.* 2 (2019) 423–430.
- [59] Y. Zou, S. Wang, *Adv. Sci.* 8 (2021), 2003579.
- [60] G.A. Cerrón-Calle, A.S. Fajardo, C.M. Sánchez-Sánchez, S. García-Segura, *Appl. Catal. B* 302 (2022), 120844.
- [61] Y. Xing, J. Ku, W. Fu, L. Wang, H. Chen, *Chem. Eng. J.* 395 (2020), 125149.
- [62] H. Chen, W. Fu, Z. Geng, J. Zeng, B. Yang, *J. Mater. Chem. A* 9 (2021) 4626–4647.
- [63] H. Chen, S. Chen, Z. Zhang, L. Sheng, J. Zhao, W. Fu, S. Xi, R. Si, L. Wang, M. Fan, B. Yang, *ACS Catal.* 12 (2022) 13482–13491.
- [64] V. Pallassana, M. Neurock, L.B. Hansen, B. Hammer, J.K. Nørskov, *Phys. Rev. B* 60 (1999) 6146–6154.
- [65] M.F. Luo, G.R. Hu, M.H. Lee, *Surf. Sci.* 601 (2007) 1461–1466.